Radio Map Estimation in the Real-World: Empirical Validation and Analysis

Raju Shrestha, Tien Ngoc Ha, Pham Q. Viet, and Daniel Romero
Department of Information and Communication Technology, University of Agder, Norway
{raju.shrestha,tien.n.ha,viet.q.pham,daniel.romero}@uia.no

***Abstract*—Radio maps quantify received signal strength or other magnitudes of the radio frequency environment at every point of a geographical region. These maps play a vital role in a large number of applications such as wireless network planning, spectrum management, and optimization of communication systems. However, empirical validation of the large number of existing radio map estimators is highly limited. To fill this gap, a large data set of measurements has been collected with an autonomous unmanned aerial vehicle (UAV) and a representative subset of these estimators were evaluated on this data. The performance-complexity trade-off and the impact of fast fading are extensively investigated. Although sophisticated estimators based on deep neural networks (DNNs) exhibit the best performance, they are seen to require large volumes of training data to offer a substantial advantage relative to more traditional schemes. A novel algorithm that blends both kinds of estimators is seen to enjoy the benefits of both, thereby suggesting the potential of exploring this research direction further.**

***Index Terms*—RF measurements, radio map estimation, unmanned aerial vehicles (UAVs), spectrum cartography.**

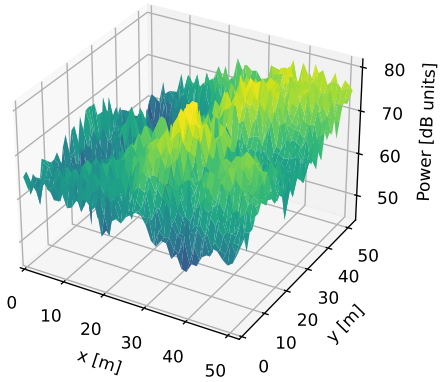

Fig. 1: 3D illustration of a power map constructed via grid discretization of one of the collected measurement sets.

I. Introduction

Radio maps characterize a radio frequency (RF) environment by providing a given metric for each spatial location [1], [2]. Examples of metrics include the received signal power, interference power, power spectral density (PSD), electromagnetic absorption, and channel gain, to name a few. Fig. 1 depicts an example of a power map. Radio maps offer therefore information about signal propagation, interference sources, and channel occupancy, which is instrumental in cellular communications, device-to-device communications, network planning, frequency planning, robot path planning, dynamic spectrum access, aerial traffic management in unmanned aerial systems, fingerprinting localization, and so on; see references in [1]. Radio maps are estimated from RF measurements collected across the area of interest.

So far, a large number of works have proposed algorithms for radio map estimation (RME); see e.g. [1], [3] and references therein. However, only a small fraction of them test their algorithms on real data. This is the case of [4], [5], [6], and [7], where power measurements were collected at respectively 700, 337, 124, and 1035 indoor locations and the performance of their algorithm was compared with a small number of benchmarks. While not adopting the most conventional RME formulation, there were studies in related problems that also collected similar datasets [8]–[11]. The largest dataset by far was collected in [9], but the algorithm proposed therein is not compared against existing ones.

Existing experimental validation is therefore rather limited, with only some works that compare the algorithm that they propose with a small number of benchmarks on small data sets. An exhaustive comparison involving a wide range of radio map estimators is still missing. To remedy this, a system was developed where an unmanned aerial vehicle (UAV) equipped with a software-defined radio collected received power measurements at more than 57,000 locations. A representative selection of existing estimators is extensively compared based on this data. The performance-complexity tradeoff and the effects of fast fading are examined by means of two problem formulations and four performance metrics. It is corroborated that estimators based on deep neural networks (DNNs) require large volumes of training data to outperform traditional interpolators. The capabilities of a novel algorithm that combines the benefits of both kinds of estimators motivate further research in this direction.

The rest of the paper is structured as follows. Sec. II reviews the RME problem along with some of the most popular schemes in the literature. Sec. III describes the data collection system and procedure used in this work. This data is then used in Sec. IV to analyze the performance of the algorithms in Sec. II. Finally, Sec. V outlines the main conclusions.

This research has been funded in part by the Research Council of Norway under IKTPLUSS grant 311994.

II. Radio Map Estimation

Although variations of the RME problem abound, the present work focuses on the two most frequent formulations, where a two-dimensional power map is estimated.

A. Model

Let $\mathcal{X} \subset \mathbb{R}^2$ comprise the Cartesian coordinates of all points in the region of interest, typically a rectangular region in a horizontal plane. A *power map* is a function that maps a location variable $\boldsymbol{x} \in \mathcal{X}$ to the received signal power (or strength) $\gamma(\boldsymbol{x})$ in a given band. This power is the result of the contribution of one or multiple transmitters. To illustrate the different factors that determine $\gamma(\boldsymbol{x})$, suppose for a moment that there is a single transmitter and that it radiates with power P_{Tx}. In this case, $\gamma(\boldsymbol{x})$ can be expressed as

$$\gamma\left(\boldsymbol{x}\right) = P_{\text{Tx}} + G - s^{\text{PL}}(\boldsymbol{x}) - s^{\text{SF}}(\boldsymbol{x}) - s^{\text{FF}}(\boldsymbol{x}), \tag{1}$$

where $s^{\text{PL}}(\boldsymbol{x}), s^{\text{SF}}(\boldsymbol{x})$, $s^{\text{FF}}(\boldsymbol{x})$, and G respectively denote the path loss, the loss due to shadow fading, the loss due to fast fading, and the constant gain term that aggregates the gains of the antennas and amplifiers.

The received power is measured by one or multiple receivers (or sensors) with isotropic antennas at N locations $\{\boldsymbol{x}_n\}_{n=1}^N \subset \mathcal{X}$. The measurement at $\boldsymbol{x}_n$ can be written as

$$\tilde{\gamma}_n = \gamma\left(\boldsymbol{x}_n\right) + z_n, \tag{2}$$

where z_n represents measurement noise.

B. Problem Formulation

Since the term $s^{\text{FF}}(\boldsymbol{x})$ in (2) is caused by multipath, it exhibits a spatial variability at a wavelength scale, which for contemporary communication systems are not greater than tens of centimeters. Thus, accurately estimating $s^{\text{FF}}(\boldsymbol{x})$ would arguably require a spacing between measurement locations below the wavelength, which would in turn require a prohibitively large number of measurements. For this reason, it is common in the RME literature to assume that fast fading is *averaged out*. Since the impact of such an assumption has never been empirically analyzed, the present work considers two common problem formulations in the literature, one where $s^{\text{FF}}(\boldsymbol{x})$ is estimated and one where $s^{\text{FF}}(\boldsymbol{x})$ is averaged out.

1) Grid-agnostic RME: In this formulation, fast-fading is not averaged out. Given the set of N measurements $\{(\boldsymbol{x}_n, \tilde{\gamma}_n)\}_{n=1}^N$, the problem is to estimate $\gamma(\boldsymbol{x})$, $\boldsymbol{x} \in \mathcal{X}$.

2) Grid-aware RME: The second formulation involves a grid discretization, which indirectly averages out fast fading and which is used by a large number of existing estimators, such as many based on deep learning, compressed sensing, and matrix completion. Consider an $N_y \times N_x$ rectangular grid $\mathcal{G} = \left\{\boldsymbol{x}_{i,j}^{\mathcal{G}}, i = 1, \ldots, N_y, j = 1, \ldots, N_x\right\} \subset \mathcal{X}$, where $\boldsymbol{x}_{i,j}^{\mathcal{G}} = [\Delta(N_y - i), \Delta(j-1)]^\top$ and Δ is the grid spacing. This assignment facilitates identifying the grid with a matrix. For each n, the measurement at $\boldsymbol{x}_n$ is assigned to the nearest grid point. Subsequently, all measurements assigned to the (i,j)-th grid point are averaged to obtain $\tilde{\gamma}_{i,j}$. The resulting measurements are then arranged in the matrix $\tilde{\boldsymbol{\Gamma}} \in \mathbb{R}^{N_y \times N_x}$, whose (i,j)-th entry equals $\tilde{\gamma}_{i,j}$ if at least one measurement has been assigned to $\boldsymbol{x}_{i,j}^{\mathcal{G}}$ and an arbitrary value (e.g. 0) otherwise. It is also convenient to form matrix $\boldsymbol{S} \in \{0,1\}^{N_y \times N_x}$, whose (i,j)-th entry equals 1 if at least one measurement has been assigned to $\boldsymbol{x}_{i,j}^{\mathcal{G}}$ and 0 otherwise. Since $\tilde{\gamma}_{i,j}$ is the average of measurements acquired typically several wavelengths away, the contribution of $s^{\text{FF}}(\boldsymbol{x})$ is significantly reduced.

The RME problem can be formulated as, given $\tilde{\boldsymbol{\Gamma}}$, estimate the power map without the fast-fading contribution, i.e.

$$\gamma_{\text{NFF}}\left(\boldsymbol{x}\right) := P_{\text{Tx}} + G - s^{\text{PL}}(\boldsymbol{x}) - s^{\text{SF}}(\boldsymbol{x}). \tag{3}$$

While a natural formulation, most grid-aware estimators can only provide estimates of $\gamma_{\text{NFF}}\left(\boldsymbol{x}\right)$ for $\boldsymbol{x} \in \mathcal{G}$.

C. Radio Map Estimators

This section briefly describes the tested estimators.

1) K-Nearest Neighbors (K-NN): This algorithm simply averages the measurements collected at the K locations with the smallest distance to the evaluation point. Specifically, given $\boldsymbol{x}$, let $\nu_k(\boldsymbol{x})$ denote the index of the k-th nearest point among $\{\boldsymbol{x}_n\}_{n=1}^N$. For example, $\nu_1(\boldsymbol{x}) = \arg\min_n \|\boldsymbol{x}_n - \boldsymbol{x}\|$ whereas $\nu_N(\boldsymbol{x}) = \arg\max_n \|\boldsymbol{x}_n - \boldsymbol{x}\|$. Although many variants exist, the simplest is to obtain $\hat{\gamma}(\boldsymbol{x}) = (1/K)\sum_{k=1}^K \tilde{\gamma}_{\nu_k(\boldsymbol{x})}$.

2) Kriging: This is a common spatial interpolation technique extensively applied to RME [2], [12]–[14]. In *simple kriging*, $\gamma(\boldsymbol{x})$ is modeled for each $\boldsymbol{x}$ as a random variable whose spatial mean $\mu_\gamma(\boldsymbol{x}) := \mathbb{E}[\gamma(\boldsymbol{x})]$ and covariance $\text{Cov}[\gamma(\boldsymbol{x}), \gamma(\boldsymbol{x}')]$ are known for all $\boldsymbol{x}$ and $\boldsymbol{x}'$. In practice, these functions are estimated from data. The simple kriging estimate is nothing but the linear minimum mean square error (LMMSE) estimator of $\gamma(\boldsymbol{x})$ based on $\tilde{\boldsymbol{\gamma}} := [\tilde{\gamma}_1, \ldots, \tilde{\gamma}_N]^\top$:

$$\hat{\gamma}(\boldsymbol{x}) = \mu_\gamma(\boldsymbol{x}) + \text{Cov}[\gamma(\boldsymbol{x}), \tilde{\boldsymbol{\gamma}}]\text{Cov}^{-1}[\tilde{\boldsymbol{\gamma}}, \tilde{\boldsymbol{\gamma}}](\tilde{\boldsymbol{\gamma}} - \mathbb{E}[\tilde{\boldsymbol{\gamma}}]), \tag{4}$$

where $\text{Cov}[\tilde{\boldsymbol{\gamma}}, \tilde{\boldsymbol{\gamma}}]$ and $\text{Cov}[\gamma(\boldsymbol{x}), \tilde{\boldsymbol{\gamma}}]$ can be found by assuming that z_n in (2) is zero-mean with variance σ_z^2 and uncorrelated with $z_{n'}$ for all $n' \neq n$ and with $\gamma(\boldsymbol{x})$ for all $\boldsymbol{x}$ [13].

3) Kernel-based Learning: Kernel-based estimators return estimates of the form $\hat{\gamma}(\boldsymbol{x}) = \sum_{n=1}^N \alpha_n \kappa(\boldsymbol{x}, \boldsymbol{x}_n)$, where the coefficients α_n depend on the specific estimator and κ is a kernel function, such as a Gaussian radial basis function of width $s > 0$, namely $\kappa(\boldsymbol{x}, \boldsymbol{x}') := \exp\{-\|\boldsymbol{x} - \boldsymbol{x}'\|^2/s\}$. One of the simplest estimators is *kernel ridge regression* (KRR), where $\{\alpha_n\}_{n=1}^N$ can be obtained in closed form by solving

$$\underset{\{\alpha_n\}_{n=1}^N}{\text{minimize}} \frac{1}{N}\sum_{n=1}^N \left|\tilde{\gamma}_n - \sum_{n'=1}^N \alpha_{n'}\kappa(\boldsymbol{x}_n, \boldsymbol{x}_{n'})\right|^2 + \rho\sum_{n=1}^N \alpha_n^2. \tag{5}$$

To reduce the influence of the kernel choice, [15] proposed a *multikernel* map estimator where the kernels in a given dictionary are combined based on the measurements.

4) Deep Learning: A large number of estimators relying on deep neural networks have been proposed [7], [8], [13], [16]–[24]. A typical approach is to concatenate $\tilde{\boldsymbol{\Gamma}}$ and $\boldsymbol{S}$ to form a $2 \times N_y \times N_x$ tensor that is passed as input to a neural network, which returns an $N_y \times N_x$ matrix $\hat{\boldsymbol{\Gamma}}$ whose (i,j)-th

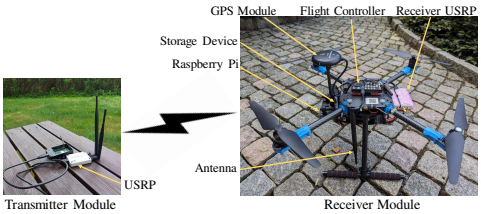

Fig. 2: Receiver and transmitter modules.

entry is an estimate for $\gamma_{\text{NFF}}(\boldsymbol{x}_{i,j}^{\mathcal{G}})$. To simplify subsequent expressions, this estimate will still be denoted as $\hat{\gamma}(\boldsymbol{x}_{i,j}^{\mathcal{G}})$.

III. Data Collection

This section details the data collection system, where the transmitter is placed at a fixed ground location and the receiver is on board a UAV with geolocation capabilities.

A. Transmitter

The transmitter (see Fig. 2) is a Universal Software Radio Peripheral (USRP) B205 mini-i with a monopole antenna of 21 cm. The USRP transmits an *orthogonal frequency-division multiplexing* (OFDM) signal with 1024 subcarriers, out of which the central 600 are used. Since the sampling rate is 5 MHz, the effective bandwidth becomes roughly 2.93 MHz. A frame that contains 12 OFDM symbols is repeatedly transmitted with a carrier frequency of 918 MHz.

B. Receiver

The receiver, which is a USRP B205 mini-i with the same antenna as the transmitter (Fig. 2) placed away from the motors to minimize the impact of self-emission [25], is installed on a quadcopter with a Raspberry Pi companion computer. The quadcopter was assembled using a Holybro X500 v2 frame and a Pixhawk 4 flight controller (FC) that runs a PX4 autopilot. The autopilot estimates the location of the vehicle by fusing the measurements of an *inertial measurement unit* (IMU) and those of a *real-time kinematic* (RTK) module, which have an accuracy of around 30 cm. The UAV follows a trajectory with a height of 7 m that comprises parallel lines spaced by 1.2 m. Such a trajectory is designed to facilitate experiments with grid quantization; cf. Fig. 3. To minimize changes in the channel due to the UAV frame, the yaw angle is kept constant.

At every second, the receiver module acquires approximately 15 uniformly-spaced sample blocks of 100,000 samples. Given that the speed is 5 m/s, the average distance between sample blocks is around 33 cm, which approximately equals the wavelength of the transmission. This is useful to average out fast fading, as described in Sec. II-B. Together with each sample block, the receiver stores the location estimates provided by the autopilot at the acquisition time.

C. Data Collection Procedure and Postprocessing

For safety reasons, the data collection takes place on a flat agricultural terrain away from residential areas. The transmitter is placed at a height of approximately 50 cm. To create different propagation conditions, one or several metallic reflectors are placed on a cardboard structure where the transmitter is located. A total of 5 measurement sets were collected, each one corresponding to a different configuration of the reflectors and orientation of the transmit antenna.

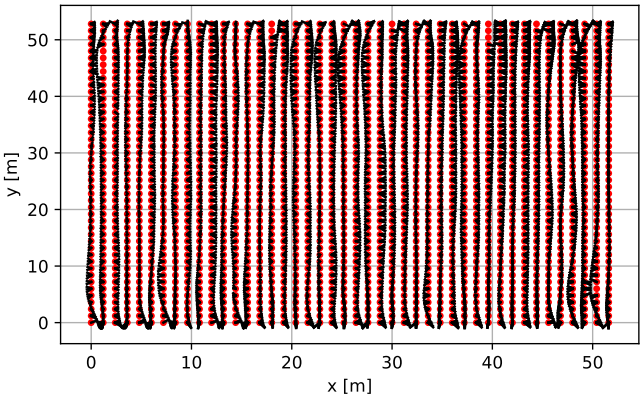

Fig. 3: Grid quantization of the measurement locations in one of the collected measurement sets. Red dots denote grid points and small black lines connect each measurement location to its nearest grid point.

The acquired sample blocks are processed offline to estimate the received power. The estimation algorithm, developed for this project, exploits the knowledge of the transmitted signal to minimize measurement error due to noise. The measurement locations are then rotated and translated to maximize alignment with the grid; cf. Fig. 3. Wind sometimes results in some grid points without assigned measurements. Yet, the alignment is sufficiently good to allow the visualization of each measurement set as in Fig. 1, where just the grid quantization procedure from Sec. II-B was applied. Observe that the ripple effect of fast fading (cf. $s^{\text{FF}}(\boldsymbol{x})$ in (1)) has not been totally averaged out as a result of the grid quantization. This effect is more apparent in Fig. 4, which plots the measurements of one column of Fig. 3 before and after grid quantization. To totally remove this effect, one could adopt a greater grid spacing Δ, but this would yield lower spatial map resolution.

IV. Experiments with Real Data

The collected data is used in this section to evaluate the performance of seven radio map estimators. Since three of them employ deep neural networks, which require large amounts of training data, one of the measurement sets is used for testing and the other four for training. For training and for Monte Carlo (MC) experiments, "patches" are generated from each measurement set by drawing an $L \times L$ square in the region uniformly at random and selecting the measurements whose locations lie inside it. After translating the measurement locations to $\mathcal{X} = [-\Delta/2, L - \Delta/2]^2$, which is where $\mathcal{G}$ is created when needed, the data is denoted as $\{(\boldsymbol{x}_n, \tilde{\gamma}_n)\}_{n=1}^{N}$. Thus, $\boldsymbol{x}_n$, $\tilde{\gamma}_n$, and N should be thought of as random variables that take new values for each patch or MC iteration.

The compared algorithms include: 1) K-NN with $K = 5$

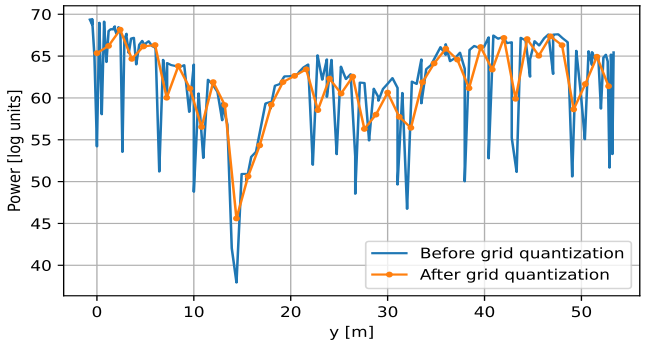

Fig. 4: Measurements in the 12-th column of Fig. 3 vs. the y-coordinate of their location. Orange: Measurements $\{\tilde{\gamma}_{i,j}\}_j$ for a fixed $j = 12$ vs. the y-coordinate of $\boldsymbol{x}^{\mathcal{G}}_{i,j}$. Blue: measurements $\{\tilde{\gamma}_n\}_n$ assigned to the points in $\{\boldsymbol{x}^{\mathcal{G}}_{i,j}\}_j$.

nearest neighbors; 2) simple Kriging with $\mathbb{E}[\gamma(\boldsymbol{x})] = 0$ and $\text{Cov}(s^{\text{SF}}(\boldsymbol{x}), s^{\text{SF}}(\boldsymbol{x}\prime)) = \sigma_s^2 2^{-\|\boldsymbol{x}-\boldsymbol{x}'\|/\delta_s}$, where $\sigma_s^2 = 9$ and $\delta_s = 50$ is the distance at which the correlation decays to $1/2$; see e.g. [13] for additional details; 3) KRR with $\rho = 10^{-3}$ and a Gaussian radial-basis function kernel with $s = 10$; 4) the multikernel algorithm in [15] with regularization parameter 10^{-3} and 3 Laplacian kernels with kernel width $s = 10, 20,$ and 30; 5) three DNN estimators.

DNN estimators construct a grid with $N_x = N_y = L/\Delta$ with $\Delta = 1.2$ m and obtain $\tilde{\boldsymbol{\Gamma}}$ and $\boldsymbol{S}$ as described in Sec. II-B2. A forward pass yields $\hat{\boldsymbol{\Gamma}}$, which provides estimates of the map at the grid locations. To obtain an estimate of the map off the grid points, the value is extracted from the estimate of the nearest grid point. Training input-output pairs are constructed by splitting $\boldsymbol{S}$ into two parts as described in Sec. IV-A2. To artificially increase the size of the training data set, data augmentation is implemented by randomly applying horizontal flipping, vertical flipping, and 90-degree rotation to the training patches. The DNNs were implemented in TensorFlow and trained with the Adam optimization algorithm with a constant learning rate of 10^{-4} and batch size 200. All three estimators use convolutional DNNs and they mainly differ in their architectures. DNN 1 follows the architecture of the mean subnetwork in [13]. With 60 M trainable parameters, it features the highest complexity. DNN 2 follows the U-Net architecture [19] with *leaky ReLU* activations, since the original tanh does not result in a good performance. With 4 M trainable parameters, its complexity is much lower than DNN 1. The DNN 3 has the same architecture as DNN 2 but the KRR estimate on $\mathcal{G}$ is concatenated to the input tensor to explore combinations between DNN-based and non-DNN estimators.

Except for the DNN estimators, all algorithms use the same parameters in all experiments. These parameters were adjusted to yield an overall good performance in all experiments. The DNN estimators, in turn, were separately trained for the two different values of L used in the experiments.

Fig. 5 shows an example of map estimation for a randomly selected patch of approximately 1,475 m^2. The number of observations, marked as black crosses, was selected so that all estimates are of a reasonable quality.

The rest of this section considers several setups to assess the performance of the considered estimators in both of the problem formulations in Sec. II-B.

A. Performance Metrics

1) Grid-agnostic Estimation: When solving the problem in Sec. II-B1, it is natural to quantify performance by the estimation error at the locations of unobserved measurements. Specifically, at each MC iteration, $\mathcal{M} := \{(\boldsymbol{x}_n, \tilde{\gamma}_n)\}_{n=1}^N$ is split into two subsets by partitioning the index set $\mathcal{N} := \{1, 2, \ldots, N\}$ into $\mathcal{N}_{\text{obs}}$ and $\mathcal{N}_{\text{nobs}}$, that is, $\mathcal{N}_{\text{obs}} \cup \mathcal{N}_{\text{nobs}} = \mathcal{N}$ and $\mathcal{N}_{\text{obs}} \cap \mathcal{N}_{\text{nobs}} = \emptyset$. The cardinality $N_{\text{obs}} := |\mathcal{N}_{\text{obs}}|$ is fixed. The measurements with index in $\mathcal{N}_{\text{obs}}$ are passed to each estimator and the returned map estimate $\hat{\gamma}(\boldsymbol{x})$ is evaluated at the locations $\{\boldsymbol{x}_n\}_{n\in\mathcal{N}_{\text{nobs}}}$. The RMSE can then be defined as

$$\text{RMSE} := \sqrt{\frac{1}{|\mathcal{N}_{\text{nobs}}|}\mathbb{E}\left[\sum_{n\in\mathcal{N}_{\text{nobs}}} |\tilde{\gamma}_n - \hat{\gamma}(\boldsymbol{x}_n)|^2\right]}, \quad (6)$$

where the expectation $\mathbb{E}$ is over patches and index sets $\mathcal{N}_{\text{obs}}$ sampled uniformly at random without replacement from $\mathcal{N}$. This sampling approach, however, may not reflect the trend in practice to have spatially clustered measurement locations. This occurs e.g. when a cellular device can collect a large number of measurements in a small part of $\mathcal{X}$ where its user remains but no measurement where its user is not present during the measurement acquisition stage. To capture this effect, define the metric $\text{RMSE}_{\mathcal{G}}$ as in (6) but with a different distribution for $\mathcal{N}_{\text{obs}}$: After creating a rectangular grid with spacing Δ, each measurement location is assigned to the nearest grid point. Then N_{obs} grid points are selected uniformly at random and $\mathcal{N}_{\text{obs}}$ is formed by collecting the indices of the measurements assigned to the selected grid points.

2) Grid-aware Estimation: When solving the problem in Sec. II-B2, it is natural to evaluate the performance on $\mathcal{G}$. To this end, at each MC iteration, $\tilde{\boldsymbol{\Gamma}}$ and $\boldsymbol{S}$ are constructed as in Sec. II-B. Let $\mathcal{N} \subset \{1, \ldots, N_y\} \times \{1, \ldots, N_x\}$ denote the set of values of (i, j) such that $[\boldsymbol{S}]_{i,j} = 1$. As before, $\mathcal{N}$ is partitioned into $\mathcal{N}_{\text{obs}}$ and $\mathcal{N}_{\text{nobs}}$, where $N_{\text{obs}} := |\mathcal{N}_{\text{obs}}|$ is given. Each estimator receives $\mathcal{N}_{\text{obs}}$ and $\{\tilde{\gamma}_{i,j}\}_{(i,j)\in\mathcal{N}_{\text{obs}}}$ and produces an estimate $\hat{\boldsymbol{\Gamma}}$. To quantify performance, consider

$$\text{RMSE}_{\text{G-nobs}} := \sqrt{\frac{1}{|\mathcal{N}_{\text{nobs}}|}\mathbb{E}\left[\sum_{(i,j)\in\mathcal{N}_{\text{nobs}}} |\tilde{\gamma}_{i,j} - \hat{\gamma}(\boldsymbol{x}_{i,j})|^2\right]}, \quad (7)$$

where $\mathbb{E}$ is over patches and over $\mathcal{N}_{\text{obs}}$, which is drawn uniformly at random over $\mathcal{N}$.

Different estimators may emphasize the spatial smoothness of their estimates to different extents. Thus, it is also insightful to consider $\text{RMSE}_{\text{G-all}}$, where $\mathcal{N}_{\text{obs}}$ is drawn in the same way as in $\text{RMSE}_{\text{G-nobs}}$ but the evaluation takes place at all grid points in $\mathcal{N}$, that is, $\mathcal{N}_{\text{nobs}}$ in (7) is replaced with $\mathcal{N}$.

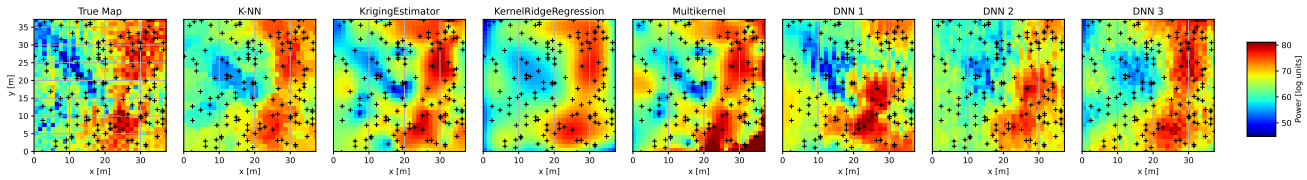

Fig. 5: True and estimates produced by the considered map estimators. Black crosses denote measurement locations.

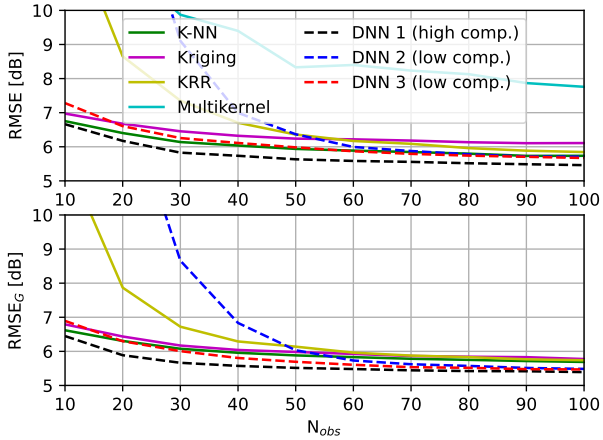

Fig. 6: Grid-agnostic performance metrics for the compared estimators vs. the number of observations when $L = 19.2$ m. The RMSE$_G$ of the multikernel estimator exceeds 10 dB and therefore it is not visible in the bottom figure.

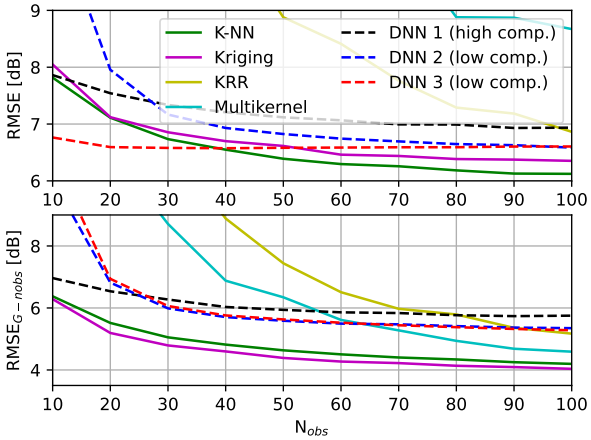

Fig. 8: Two of the considered performance metrics vs. the number of observations when $L = 38.4$ m.

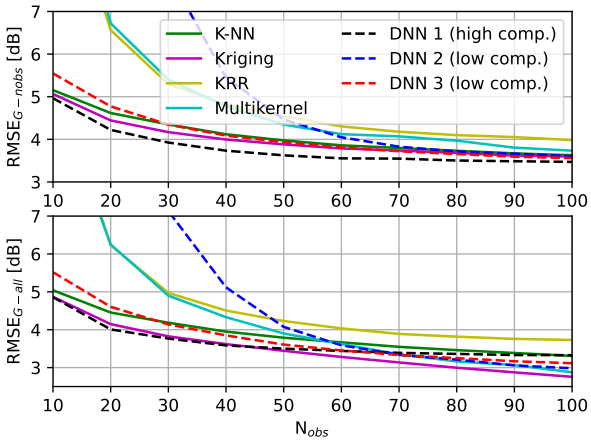

Fig. 7: Grid-aware performance metrics for the compared estimators vs. the number of observations when $L = 19.2$ m.

B. Monte Carlo Experiments

The metrics in Sec. IV-A are obtained next using MC experiments where, at each iteration, a patch and a sampling set $\mathcal{N}_{\text{obs}}$ are generated as described there.

Figs. 6 and 7 depict these metrics when the patch side is $L = 19.2$ m. This ensures that the test set contains a sufficiently high number of distinct patches and the training set is sufficiently large for DNN training. It is observed in Fig. 6 that the RMSE of the best estimators approximately attains its lowest value with just 30 observations, which amounts to one observation for every 12 m^2. From Fig. 7, RMSE$_{\text{G-nobs}}$ requires a few more observations to attain the final value, but this final error is lower. Note that, due to its definition, RMSE$_{\text{G-all}}$ will continue decreasing until $N_{\text{obs}} = N$ for any reasonable estimator. Even the trivial estimator that returns $\hat{\gamma}(\boldsymbol{x}_{i,j}^{\mathcal{G}}) = \tilde{\gamma}_{i,j}$ for all i, j will attain RMSE$_{\text{G-all}} = 0$ when $N_{\text{obs}} = N$. Overall, the estimation error of most estimators is around 6 dB for the grid-agnostic metrics, whereas it may be as low as 3.5 dB for RMSE$_{\text{G-nobs}}$. This agrees with intuition: averaging out fast fading reduces the spatial variability of $\gamma(\boldsymbol{x})$, which renders it an easier function to estimate. The best-performing algorithms are based on DNNs. However, simple algorithms such as K-NN and Kriging offer highly competitive performance. This suggests that the benefits of using DNN estimators may not be worth the performance gain. Nonetheless, the performance gap is likely to increase if the DNNs are trained with more data. It is also important to keep in mind that the same parameters were used for each algorithm in all points of Figs. 6 and 7. Improved performance must be expected if such parameters are set depending on N_{obs}.

Fig. 8 shows the MC estimates of the metrics in (6) and (7) when $L = 38.4$ m. The comparison is not as reliable as the one in Figs. 6 and 7 since the number of distinct test patches

is now just 156. Remarkably, the number of observations per m^2 to attain RMSE $\approx$ 6 dB is roughly the same as in Fig. 6. $\text{RMSE}_{\text{G-nobs}}$ is also similar to the one in Fig. 7 for a sufficiently large number of observations. The performance of the DNN estimators is severely degraded with respect to Figs. 6 and 7 because the larger L dramatically reduces the number of training patches. Interestingly, DNN 3 yields the best RMSE for a low N_{obs}. This highlights the potential of hybrid algorithms that combine DNN estimators with more traditional interpolation techniques such as KRR.

V. Conclusions

This paper assesses the performance of a representative subset of existing radio map estimators on real data collected with a UAV. Two RME problem formulations were considered and the quality of the estimates was assessed by means of four performance metrics.

One of the most remarkable observations is the overall good performance of simple estimators such as K-NN or Kriging. This fact may have gone unnoticed in a large part of the literature, where sophisticated estimators are proposed but no comparisons with such benchmarks are presented. One experiment also revealed the potential of combining DNN estimators and interpolators. It was also observed that averaging out fast fading greatly facilitates estimation.

Among the limitations of the present study, one may highlight the following: 1) although the number of measurement locations in the dataset is by far the largest in the literature, it is still insufficient to train the "data-hungry" DNN estimators. A larger performance gain relative to traditional estimators must be expected when DNN estimators are trained on more data. 2) All estimators used the same parameters in all experiments. Performance improvements may be expected if they are adjusted depending on the target metric and N_{obs}. 3) Only power maps were considered, so estimators for other classes of maps are yet to be investigated. 4) All measurements took place in the same frequency band, so some conclusions may not carry over to other parts of the RF spectrum.

Future work will include more extensive data collection, a more systematic optimization of the parameters of traditional estimators, consideration of other classes of maps, and the development of further hybrid estimators that combine DNNs and more traditional approaches.

References

[1] D. Romero and S.-J. Kim, "Radio map estimation: A data-driven approach to spectrum cartography," *IEEE Signal Process. Mag.*, Nov. 2022.

[2] A. Alaya-Feki, S. B. Jemaa, B. Sayrac, P. Houze, and E. Moulines, "Informed spectrum usage in cognitive radio networks: Interference cartography," in *Proc. IEEE Int. Symp. Personal, Indoor Mobile Radio Commun.*, Cannes, France, Sep. 2008, pp. 1–5.

[3] M. Höyhtyä, A. Mämmelä, M. Eskola, M. Matinmikko, J. Kalliovaara, J. Ojaniemi, J. Suutala, R. Ekman, R. Bacchus, and D. Roberson, "Spectrum occupancy measurements: A survey and use of interference maps," *IEEE Commun. Surveys Tutorials*, vol. 18, no. 4, pp. 2386–2414, 2016.

[4] Z. Xiang, H. Zhang, J. Huang, S. Song, and K.C. Almeroth, "A hidden environment model for constructing indoor radio maps," in *IEEE Int. Symp. World Wireless Mobile Multimedia Net.*, 2005, pp. 395–400.

[5] Y. Hu, W. Zhou, Z. Wen, Y. Sun, and B. Yin, "Efficient radio map construction based on low-rank approximation for indoor positioning," *Math. Probl. Eng.*, vol. 2013, 2013.

[6] B. Yang, S. He, and S.-H. G. Chan, "Updating wireless signal map with Bayesian compressive sensing," in *Proc. ACM Int. Conf. Mod., Anal. and Simu. Wireless and Mobile Sys.*, New York, NY, USA, 2016, MSWiM '16, pp. 310–317, Association for Computing Machinery.

[7] Q. Niu, Y. Nie, S. He, N. Liu, and X. Luo, "RecNet: A convolutional network for efficient radiomap reconstruction," in *IEEE Int. Conf. Commun.*, 2018, pp. 1–7.

[8] C. Parera, Q. Liao, I. Malanchini, C. Tatino, A. E. C. Redondi, and M. Cesana, "Transfer learning for tilt-dependent radio map prediction," *IEEE Trans. Cognitive Commun. Netw.*, vol. 6, no. 2, pp. 829–843, Jan. 2020.

[9] T. Hayashi, T. Nagao, and S. Ito, "A study on the variety and size of input data for radio propagation prediction using a deep neural network," in *Proc. IEEE European Conf. Antennas Propag.*, Copenhagen, Denmark, Jul. 2020, IEEE, pp. 1–5.

[10] E. Ostlin, H.-J. Zepernick, and H. Suzuki, "Macrocell path-loss prediction using artificial neural networks," *IEEE Trans. on Veh. Technol.*, vol. 59, no. 6, pp. 2735–2747, 2010.

[11] S. I. Popoola, A. Jefia, A. A. Atayero, O. Kingsley, N. Faruk, O. F. Oseni, and R. O. Abolade, "Determination of neural network parameters for path loss prediction in very high frequency wireless channel," *IEEE Access*, vol. 7, pp. 150462–150483, 2019.

[12] A. Agarwal and R. Gangopadhyay, "Predictive spectrum occupancy probability-based spatio-temporal dynamic channel allocation map for future cognitive wireless networks," *Trans. Emerging Telecommun. Technol.*, vol. 29, no. 8, pp. e3442, 2018.

[13] R. Shrestha, D. Romero, and S. P. Chepuri, "Spectrum surveying: Active radio map estimation with autonomous UAVs," *IEEE Trans. Wireless Commun.*, Aug. 2022.

[14] G. Boccolini, G. Hernandez-Penaloza, and B. Beferull-Lozano, "Wireless sensor network for spectrum cartography based on kriging interpolation," in *Proc. IEEE Int. Symp. Personal, Indoor Mobile Radio Commun.*, Sydney, NSW, Nov. 2012, pp. 1565–1570.

[15] J.-A. Bazerque and G. B. Giannakis, "Nonparametric basis pursuit via kernel-based learning," *IEEE Signal Process. Mag.*, vol. 28, no. 30, pp. 112–125, Jul. 2013.

[16] T. Imai, K. Kitao, and M. Inomata, "Radio propagation prediction model using convolutional neural networks by deep learning," in *Proc. IEEE European Conf. Antennas Propag.*, Krakow, Poland, Apr. 2019, IEEE, pp. 1–5.

[17] M. Iwasaki, T. Nishio, M. Morikura, and K. Yamamoto, "Transfer learning-based received power prediction with ray-tracing simulation and small amount of measurement data," *arXiv preprint arXiv:2005.00833*, 2020.

[18] Y. Teganya and D. Romero, "Deep completion autoencoders for radio map estimation," *IEEE Trans. Wireless Commun.*, 2021.

[19] E. Krijestorac, S. Hanna, and D. Cabric, "Spatial signal strength prediction using 3D maps and deep learning," in *Proc. IEEE Int Conf. Commun.* IEEE, 2021, pp. 1–6.

[20] J. Thrane, D. Zibar, and H. L. Christiansen, "Model-aided deep learning method for path loss prediction in mobile communication systems at 2.6 GHz," *IEEE Access*, vol. 8, pp. 7925–7936, 2020.

[21] V. V. Ratnam, H. Chen, S. Pawar, B. Zhang, C. J. Zhang, Y.-J. Kim, S. Lee, M. Cho, and S.-R. Yoon, "FadeNet: Deep learning-based mm-wave large-scale channel fading prediction and its applications," *IEEE Access*, vol. 9, pp. 3278–3290, 2020.

[22] R. Levie, Ç. Yapar, G. Kutyniok, and G. Caire, "RadioUNet: Fast radio map estimation with convolutional neural networks," *IEEE Trans. Wireless Commun.*, vol. 20, no. 6, pp. 4001–4015, 2021.

[23] X. Han, L. Xue, F. Shao, and Y. Xu, "A power spectrum maps estimation algorithm based on generative adversarial networks for underlay cognitive radio networks," *Sensors*, vol. 20, no. 1, pp. 311, Jan. 2020.

[24] S. Shrestha, X. Fu, and M. Hong, "Deep generative model learning for blind spectrum cartography with NMF-based radio map disaggregation," in *Proc. IEEE Int. Conf. Acoust., Speech, Signal Process.* IEEE, 2021, pp. 4920–4924.

[25] H. Pienaar, J . A. Andriambeloson, and D. B. Davidson, "Rf shielding for multi-copter based electromagnetic metrology platforms," in *2016 IEEE Conf. on Antenna Meas. & Appl. (CAMA)*. IEEE, 2016, pp. 1–4.